Thermally Driven SOFC Degradation in 4D: Part II. Macroscale

T. M. M. Heenan, X. Lu, J. B. Robinson, F. Iacoviello, D. J. L. Brett, and P. R. Shearing[z]

Electrochemical Innovation Lab, Department of Chemical Engineering, UCL, London WC1E 7JE, United Kingdom

An inability to withstand rapid thermal cycling remains a major challenge for solid oxide fuel cells (SOFCs). Delamination of the anode and electrolyte layers due to mismatch in the thermal expansion coefficients (TEC) is a significant source of degradation. The first part of these studies inspected the interactions at the microscale, while this work presents the second of the two-part study and investigates such degradation with a focus on the macroscale. During thermal cycling the cell walls contracted and the interface concaved. A critical transition is thought to be triggered by an upper limit on the thermal ramp-rate, which in this case relates to rates above $20°C{\cdot}min^{-1}$. Additionally, the interfacial contact was observed to reduce with each thermal cycle progressing linearly until the aforementioned critical point was reached, after which a significant reduction in the degradation rate was observed. Interfacial curvature may also be responsible for cracking within the anode layer due to the localized tensile strain experienced during the bending process. This two-part study presents the first extended 4D investigation into the effects of thermal cycling at sub-micron resolution using only lab-based instruments. These results present valuable insight into interfacial delamination and anode cracking important in both cell design and operation.

 [DOI: 10.1149/2.0061811jes]

Manuscript submitted May 14, 2018; revised manuscript received July 19, 2018. Published August 11, 2018.

Fuel cells are promising devices for energy conversion,[1] particularly, high temperature fuel cells such as the solid oxide fuel cell (SOFC) offer high net efficiencies, fuel versatility and fast reaction kinetics, without the need for expensive metal catalysts. However, reductions in performance throughout the lifetime of the cell due to complex degradation mechanisms continue to inhibit their widespread commercialization.[2]

One well-known mechanism of SOFC degradation is the delamination of the electrolyte from the anode electrode. Delamination of the two layers is particularly problematic in planar cells and is attributed to the mismatch in the thermal expansion coefficient (TEC) between the electrolyte and anode layers during operational thermal cycling.[3] Efforts have been made to combat such deviations through the use of various support types combined with the addition of the ceramic electrolyte to the metal anode in the formation of cermet materials, this has the dual benefit of also increasing the reaction site density within the electrode.[4]

Nickel (Ni) is a commonly employed anode material with 8 mol% yttria-stabilized zirconia (YSZ) ceramic as the electrolyte, forming Ni-YSZ as the cermet anode material. Bulk TEC values for Ni, Ni-YSZ and YSZ are approx. 16, 12 and 10×10^{-6} $°C^{-1}$, respectively, through the temperature ranges typical of SOFC operation.[5–8] Evidently employing cermet anode materials does reduce the macroscopic TEC difference, although microscopically the disparity in TEC remains problematic.[9–12]

Contact between the anode and electrolyte is imperative to allow the transport of O^{2-} ions from the reduction of oxygen at the cathode reaction sites, thought the electrolyte to the oxidation with hydrogen forming water at the anode reaction sites. The reaction sites within the anode are widely accepted to be located at the triple-phase boundary (TPB) point, the location where the three transport processes: ionic, electronic and gaseous, come into contact.[4] These three transport routes occur in the ceramic, metallic and porous networks.

The mapping and quantification of such reaction sites has become widespread in recent years, owing to the advancements in 3D materials characterization tools. Initially focused-ion beam scanning electron microscopes (FIB-SEMs) were used to characterize features such as the TPB[13] and the anode/electrolyte contact,[2] although this requires the destruction of the sample, preventing repeated analysis. By contrast X-ray computed tomography (CT) allows the characterization of 3D structures without the destruction of the sample, permitting studies of the same region of interest (ROI)[14] while maintaining a large field of view (FOV). Until recent years, such techniques would require the use of limited-access synchrotron facilities but improvements in lab-based equipment[15] has resulted in competitive spatial resolution and the possibility of long duration studies.

Although anode fabrication and characterization methods are improving[16–19] the reduction in the interfacial contact continues to impede performance[3,2] and remains insufficiently understood. Furthermore, in order to find entry to the mass-market, portable SOFC applications will require rapid start-up and shut-down times to be comparable with competing technologies. In order to achieve this high thermal ramp-rates must be employed which accelerate degradation and reduce cell lifetime. It is therefore of great importance to improve understanding of the mechanisms which lead to, and result from, electrolyte delamination as improved understanding will ultimately lead to enhanced mitigation strategies through intelligent cell designs and improved operation procedures.

The structural evolution of two layers with different TECs exposed to thermal cycling is well understood and can be predicted by Timoshenko's model for a bi-material strip.[20] The metal/ceramic and cermet/ceramic interactions have also been investigated extensively through a host of materials characterization techniques[12,13] postulating the initiation and propagation of cracking as observed by analogous studies[21] although, extended studies on the interfacial performance with operational cycling remain limited.[22–24]

This work presents the first long-duration investigation into the change in interfacial contact between the anode and electrolyte within an anode supported SOFC using sub-micron X-ray CT. By inspecting both surface and internal features at high resolution, this work provides a comprehensive study into the causes and effects of interfacial contact loss with thermal cycling, and the possible repercussions on the electrochemical performance of the cell. These studies may also provide as a basis for future work on analogous materials where delamination mechanisms inhibit material performance.

Experimental

Materials and sample preparation.—The cell investigated here was an anode supported, anode/electrolyte solid oxide half-cell (Fuel Cell Materials, OH, USA) with a nickel oxide (NiO) - 8mol% yttria stabilized zirconia (8YSZ) cermet anode (NiO-8YSZ) and 8YSZ ceramic electrolyte, each ca. 500 μm and 10 μm in thickness, respectively. In order to collect 3D microstructures of sufficient resolution, a sample was extract from the half-cell using an A Series/Compact Class 4 532 nm Laser Micromachining System (Oxford Lasers,

[z]E-mail: p.shearing@ucl.ac.uk

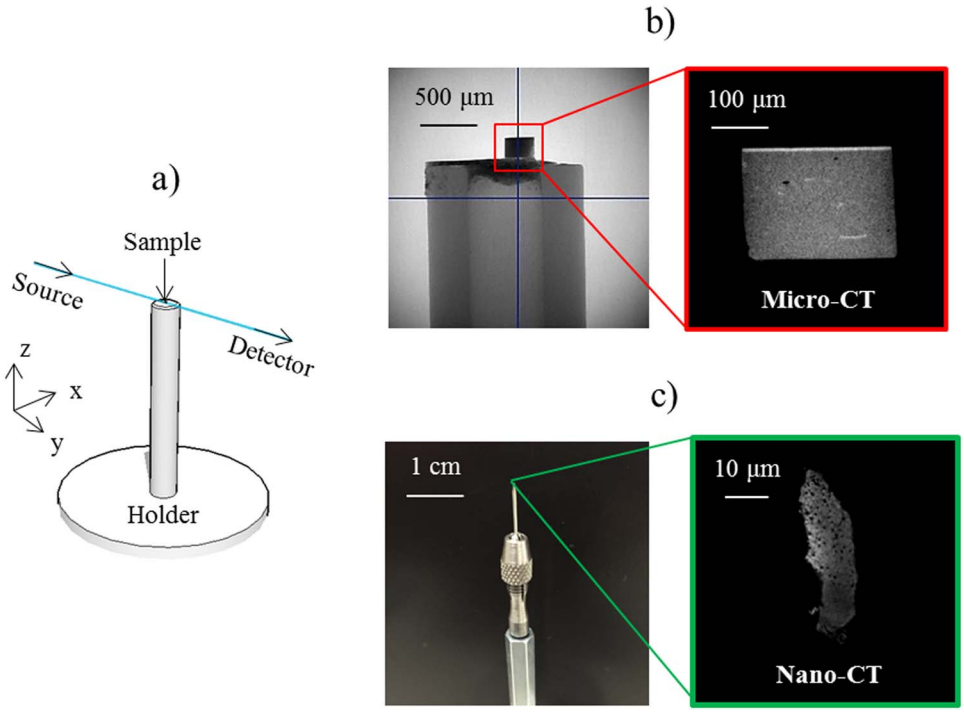

Figure 1. Multiple length-scale X-ray computed tomography: a) Spatial orientation of the X-ray beam-path, b) low magnification radiograph of the sample and support-mount with accompanying reconstructed micro-CT ortho-slice and, c) photograph of the sample mounted for nano-CT with accompanying reconstructed nano-CT ortho-slice.

Oxford, UK). First, a cylindrical sample with diameter ca. 800 µm was removed from the cell bulk and attached to an alumina tube using high-temperature cement, a technique which was developed and reported previously by the authors,[25,26] and finally refined to ca. 350 µm in diameter, this technique is also explored thoroughly elsewhere.[27]

In order to collect high-resolution post-mortem data the sample was reinserted into the micromachining system and a sub-sample, ca. 10 µm in diameter and 30 µm in height, was cut from the bulk for analysis.

Thermal cycling and X-ray CT.—X-ray CT was conducted at two length scales through the use of micro- and nano-CT, as seen in Figure 1. Before conducting microstructural analysis, the metal within the anode cermet was reduced to nickel (Ni) at 800°C in a forming gas atmosphere (4% H_2 96% N_2) held for two hours and allowed to cool via natural convection (Cycle 1 in Figure 2a). The Ni-8YSZ/8YSZ sample was then sequentially exposed to thermal cycling (Cycles 2–15 in Figure 2a). 3D microstructural information was obtained before and after each cycle using a lab-based X-ray micro-CT instrument (Zeiss Xradia 520 Versa, Carl Zeiss., CA, USA), with an isotropic pixel length of 395 nm and field of view (FOV) of 384 µm (sample set-up is displayed in Figure 1 and the gray volume renders of each tomograms indicated by red arrows in Figure 2c). Images were acquired with a 40× optical magnification and a binning of two. Thermal cycles were all conducted from room temperature to 750°C in a forming gas atmosphere although with each thermal cycle the heating ramp-rate was increased: 3, 10, 20 and 30°C·min^{-1} respectively. An accelerated stress test was then completed at 30°C·min^{-1} accumulating 15 total thermal cycles with tomograms collected every five thermal cycles. On completion of the 15th thermal cycle a post-mortem sub-sample, ca. 10 µm in diameter and 30 µm in height, was inspected with use of a lab-based X-ray nano-CT instrument (Zeiss Xradia 810 Ultra, Carl Zeiss., CA, USA), with an isotropic pixel length of ca. 126 nm, (Figures 1b and 1c) with a FOV of ca. 64 µm. The X-ray CT scanning parameters and thermal treatment conditions can be found in Table I and Table II, respectively, and visualized in Figure 2. The micro- and nano-CT radiographs were reconstructed using filtered back projection algorithms using commercial software ('Reconstructor Scout-and-Scan', Carl Zeiss., CA, U.S.A.).

Deformation.—The deformation of the cell was quantified by four metrics: electrolyte thickness (t), cell-wall angle (θ), horizontal (Δx) and vertical (Δz) displacements (see Figure 3a for geometric reference). The angular and horizontal displacement quantifies the contraction of the cell wall perpendicular to the anode/electrolyte interface, whereas the vertical displacement describes the magnitude of the cell curvature. These metrics were quantified with use of the angular and 3D length measurements conducted on the greyscale data in Avizo Fire software (Avizo, Thermo Fisher Scientific, Waltham, Massachusetts, U.S.).

Delamination.—Sub-volumes were taken across the radius from the cell center to cell-wall within each of the tomograms (See Figures 3a and 2b). These sub-volumes were subsequently segmented, through greyscale thresholding, into three materials: anode (Ni-YSZ), electrolyte (YSZ) and pore. The volume specific interfacial contact area between the solid-anode and solid-electrolyte layers (A) was then quantified using a MATLAB application, TauFactor[28] (See Figure 3c). Care was taken to ensure that the sub-volumes were taken perpendicular to the anode/electrolyte interface, accounting for interfacial curvature (Figure 3a). The delamination, quantified by the anode-electrolyte contact, is dependent upon the quality of the segmentation, it is therefore imperative that sufficient rigor is ensured during distinction of the anode from the electrolyte. The pixel size is 395 nm in length, and the features at the interface are on the order of several microns, the extracted data from these features is averaged for a sub-volume on the order of hundreds of microns therefore sufficient confidence in the delamination quantification has been ensured.

Crack propagation.—The micro- and nano-scale cracking was quantified by segmentation of the crack and mapping of a central path. Segmentation was achieved by cropping a volume which tightly enclosed the meander of a crack path, followed by the segmentation

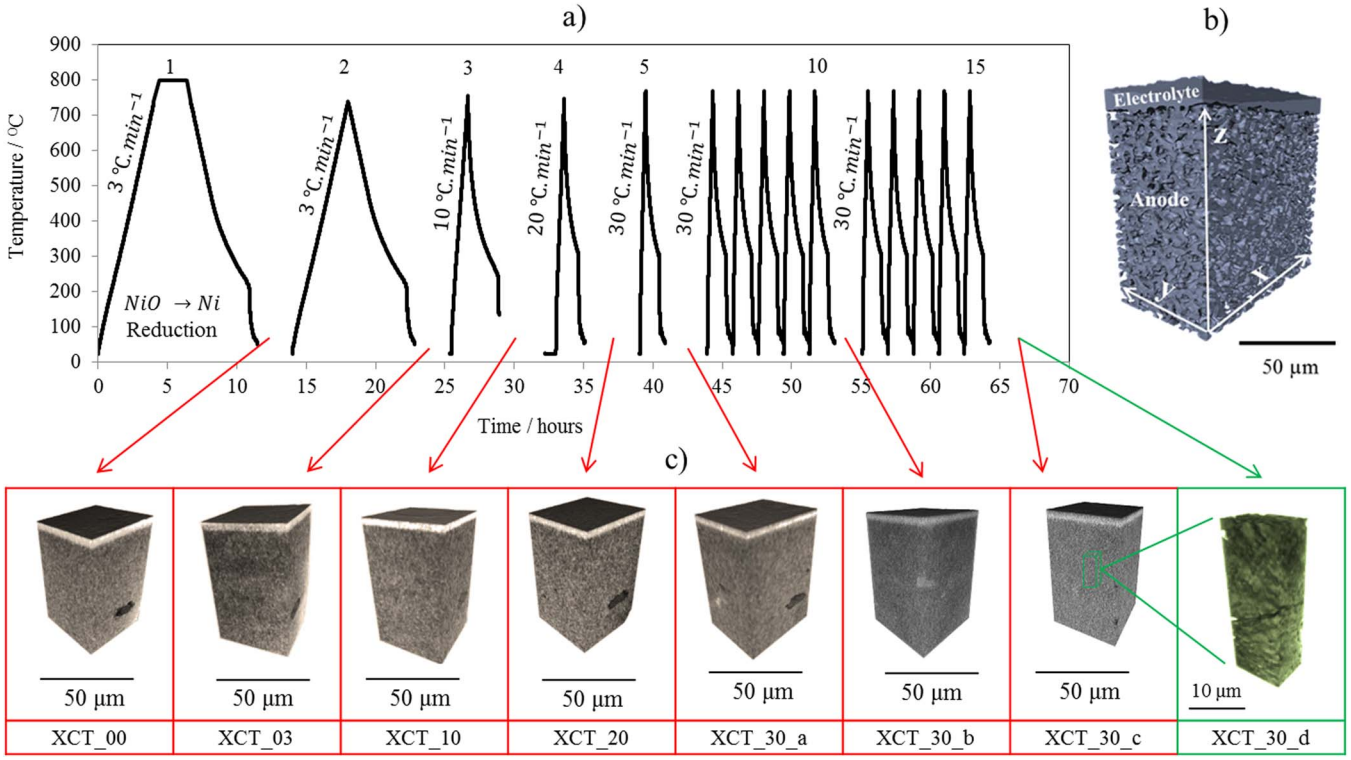

Figure 2. Furnace conditions for the thermal cycling of an anode supported solid oxide half-cell examined via multiple length-scale X-ray computed tomography: a) temperature profile with reference to when tomograms were collected, b) sample solid-volume surface rendering for reference of spatial orientations, and c) greyscale volume renders of sub-volumes taken from each tomogram. Throughout red and green respectively indicate micro- and nano-CT.

Table I. X-ray imaging conditions for the X-ray CT tomograms obtained from the anode-supported solid oxide half-cell using the lab-based 520 Versa micro-CT and 810 Ultra nano-CT X-ray instruments.

	Micro-CT	Nano-CT
Lab-based Instrument	520 Versa	810 Ultra
Radiograph Projections/images	2401	1101
Exposure Time/seconds	30	45
Pixel Size/nm	395	126
Binning/no-units	2	2
Field of View/µm × µm	384 × 384	64 × 64
Sample Volume Analyzed/µm^3	2 × 10^7	2 × 10^5
Source Energy/keV	58.0	5.4

Table II. Thermal cycling conditions for the eight X-ray CT tomograms with the number of thermal cycles between each tomography, the total number of accumulated thermal cycles and the constant heating ramp-rate.

Number	Data Set	Instrument	Thermal Cycles Accumulated	Ramp rate/ °C·min^{-1}
1	XCT_00	VERSA	1	3
2	XCT_03	VERSA	2	3
3	XCT_10	VERSA	3	10
4	XCT_20	VERSA	4	20
5	XCT_30_a	VERSA	5	30
6	XCT_30_b	VERSA	10	30
7	XCT_30_c	VERSA	15	30
8	XCT_30_d	ULTRA	15	-

of all pores (including cracks) again, with use of a greyscale threshold with reference to the greyscale of the space surrounding the sample (Figure 7a). Once all the porous phase was segmented a 'top-hat' transform was computed on the image, allowing the distinction of cracks from the pore.[29] A central skeleton of the crack network was then mapped in 3D using Avizo's 'Auto-Skeleton' algorithm which employs a medial axis-based method using distance ordered homotopic thinning (DOHT)[30] to determine the phase diameter by calculating the distance between the skeleton to the phase boundary. Detailed descriptions of such algorithms can be found elsewhere.[31] The local crack diameter (Ø) was then inspected with the accompanying crack length (l) and finally a crack-diameter histogram with a binning of 126 nm was calculated. This analysis was performed for both the micro- and nano-tomograms which were acquired from the sample as a post-mortem analysis after the fifteenth thermal cycle. To compare the two length scales, three cracks were analyzed from each of the two tomograms, totalling six propagated cracks. To inspect the crack propagation, the minimum, maximum, average and standard deviation of the crack diameters were computed for each crack and assessed with respect to the respective crack length.

Results

Cell-wall contraction and electrolyte curvature.—Significant horizontal wall contraction is observed after thermal cycling (Figures 4a and 4b), resulting in a horizontal displacement of 20.8 µm and contraction of the cell-wall by 7.5°. Substantial vertical displacement is also observed after cycling, 6.6 µm (Figures 4c and 4d), producing a curvature comparable to values reported previously[9] (Figure 4e). The transition point for both the horizontal and vertical displacements occurs after the fifth thermal cycle in both orientations (Figures 4f and 4g). The fifth thermal cycle is the first to exceed 20°C·min^{-1}. The relationship between structural performance and the thermal ramp-rate employed is well recognized: high thermal ramp-rates induce a higher degree of thermal shock and exacerbates thermal expansion mismatch

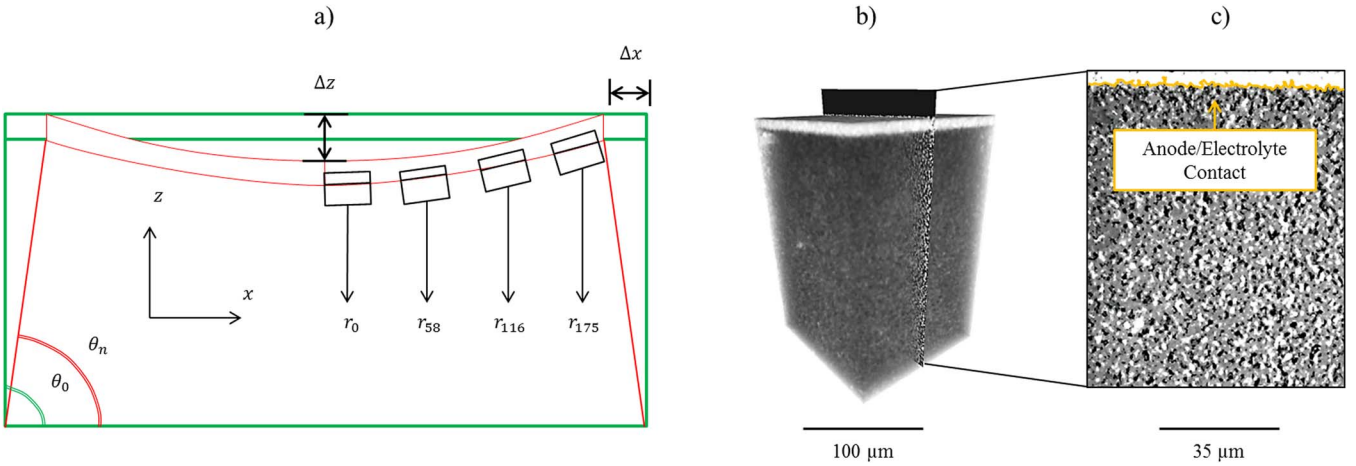

Figure 3. Geometric orientations for the quantification of the cell deformation: a) a schematic outlining the cell-wall angle (θ), horizontal (x) and vertical (z) cell displacement, b) a greyscale volume render of a sub-volume taken from the pristine sample at the center of the cell, and c) a single slice from the same sub-volume with the anode-electrolyte contact area indicated in orange.

between the constituent materials. However, the propagation of such shock is not well-known for real microstructures. Here it is observed that at low low ramp-rates, deformation is plastic but negligible, deforming less than 3 μm in both orientations, similarly, once high ramp-rates are achieved deformation proceeds plastically but again no more than 3 μm. These two deformation developments are separated by a substantial deformation triggered by the fifth thermal cycle (Figure 4f). This may indicate that a critical yield-point is irreversibly triggered once a sufficiently high thermal ramp-rate is exceeded, which in this case relates to rates above 20°C·min^{-1}.

Although the horizontal displacement is measured at the anode/electrolyte interface, the deformation of the cell support layer is also inspected through the quantification of the angle between the cell-wall and the cell-face which would be in contact with the anode flow channels and current collector. The cell contraction angle, the angle by which the cell-wall changes with respect to the initial structure, follows a similar profile (Figure 4h) to that of the horizontal and vertical displacements. However, the transition occurs more gradually suggesting that strain may not be uniform throughout the anode layers, this has been suggested by anode supported cells in previous literature.[11] Quantification of the cell deformations is presented in Table III.

Negligible variation was observed in the electrolyte thickness across the cell radius. The electrolyte thickness was found to be relatively consistent with thermal cycling apart from the third, fourth and fifth cycles where the electrolyte thickness was recorded to increase by ca. 1 μm. These variations are very small with respect to the resolution off the datasets but large with respect to the electrolyte thickness and are presented consistently. This deviation is observed prior to the aforementioned critical yield point and may be a result of tension within the electrolyte which accumulated before the severe cell curvature and contraction. This finding may be validated in future work using crystallographic information, as such techniques may provide further information on this tensile/compression mechanism but is considered beyond the scope of this publication.

Anode/electrolyte delamination.—The cell delamination is assessed by the loss of contact area between the anode and electrolyte layers, this is visualized in Figure 5. Inspecting the anode/electrolyte contact for each tomogram (Figure 5d) it is clear that the contact decreases by a quasilinear trend until the thermal ramp-rate is no longer increased, at which point the contact reduces at a substantially reduced rate. This resulted in a contact reduction of 80% after completion of the cycling profile, although 69% of this was established during the first five cycles (Figure 5e). Again, when inspected with respect to the cell-wall contraction (Figure 5f) the decrease is more gradual, suggesting a non-uniform strain distribution within the cell. When compared to the cell wall displacements (Figure 5g) it is evident that the interfacial contact has reduced significantly (ca. $50-60\%$) before the substantial cell deformation occurs. As mentioned in the previous section this would suggest that strain accumulates within the cell during thermal cycling until the critical yield transition occurs. The average volume-corrected anode/electrolyte contact area and reduction with respect to the initial interfacial contact is reported in Table IV.

Non-uniform degradation.—As discussed, the average anode/electrolyte contact area is observed to reduce with thermal cycling although, the deformation observed in the form of electrolyte curvature and cell-wall contraction suggests non-uniform strain may be accumulating within the anode layers. Figure 6 displays the location of multiple sub-volumes which were extracted from each tomogram at four points along the cell radius from the center to cell-wall, r_0, r_{58}, r_{116} and r_{175}, denoted as such according to the radial position: 0, 58, 116 and 175 μm. Inspecting the variation across

Table III. Cell deformations as a result of thermal cycling to 750°C quantified by the cell wall angle, horizontal and vertical displacements.

Thermal Cycles/no-units	1	2	3	4	5	10	15
Thermal Ramp Rate/°C·min^{-1}	3	3	10	20	30	30	30
Cell wall Angle/degrees	88.4	88.2	88.0	86.1	84.8	84.1	80.9
Cell Contraction/degrees	0.0	0.2	0.4	2.3	3.6	4.3	7.5
Horizontal displacement/μm	0.0	0.0	0.0	2.0	16.6	17.7	20.8
Vertical displacement/μm	0.0	0.0	0.6	0.7	6.0	6.2	6.6
Change in Horizontal displacement/μm	N/A	0.0	0.0	2.0	14.5	1.1	3.2
Change in Vertical displacement/μm	N/A	0.0	0.6	0.1	5.4	0.2	0.4

Table IV. Average interfacial contact area volume corrected including the reduction in contact area with respect to the initial sample structure.

Thermal Cycles/no-units	1	2	3	4	5	10	15
Thermal Ramp Rate/°C·min^{-1}	3	3	10	20	30	30	30
Average anode/electrolyte specific contact area/μm^{-1}	0.13	0.10	0.08	0.06	0.04	0.04	0.03
Reduction in contact area/%	0	27	43	54	69	70	80

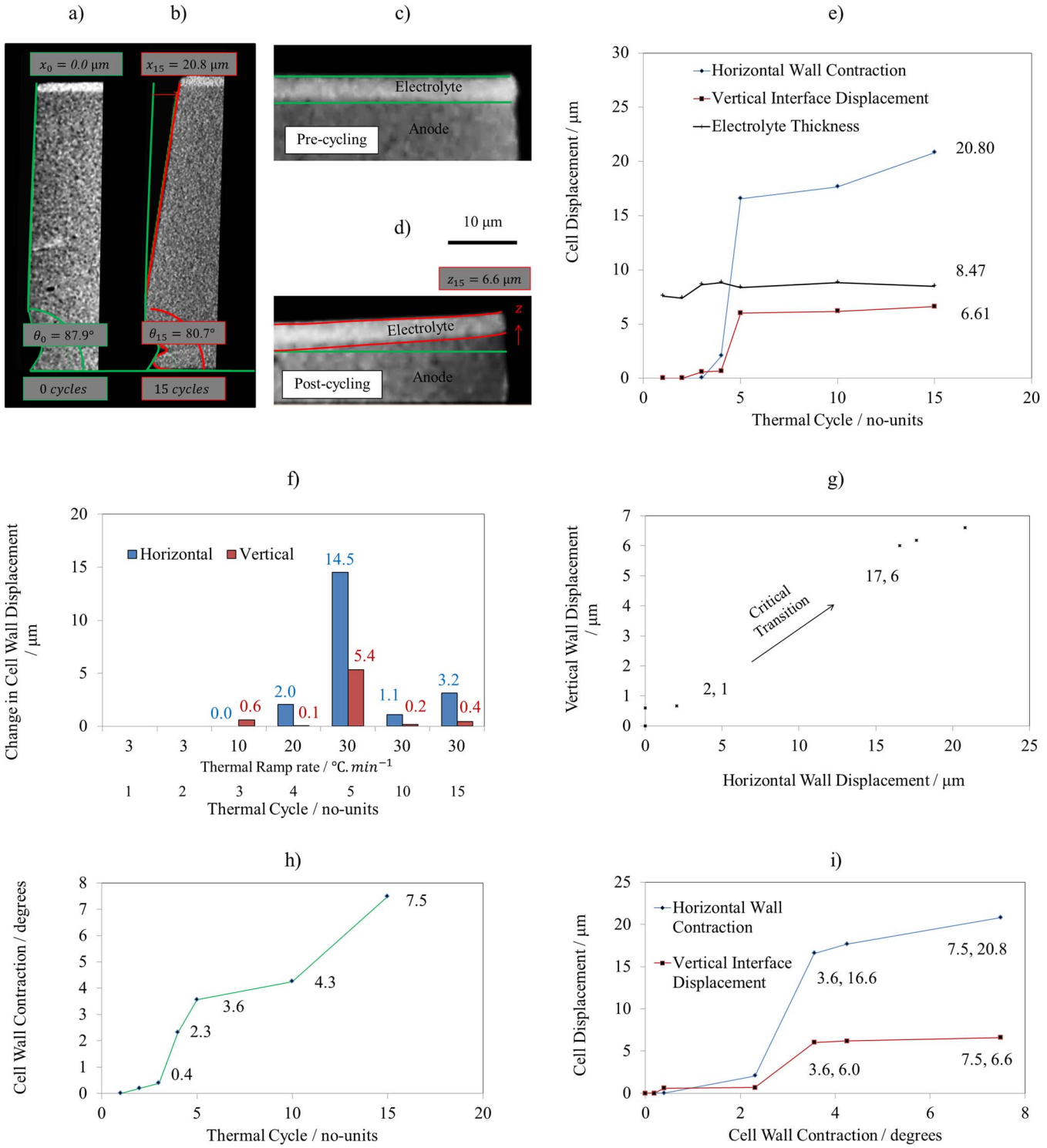

Figure 4. Deformations as a result of operational thermal cycling to 750°C: X-ray tomogram slices in the x-z plane for a) 1 cycle, b) 5 cycles, c) 10 cycles and d) 15 cycles, magnification of the e) 1 cycle and f) 15 cycles inspecting the interfacial delamination, g) horizontal and vertical cell displacement with accompanying electrolyte thickness, h) comparison of the horizontal and vertical displacement with critical transition, i) cell-wall contraction angle with respect to the number of thermal cycles, and j) the horizontal and vertical cell displacements inspected with respect to the cell-wall contraction angle.

the cell, there is a reduction in the interfacial contact area across the cell radius which increases with each thermal cycle; initially, the difference between the cell-center and cell-wall was below 1% but after cycling the difference rises to over 2% (Figure 6e). Again vertical displacement only occurs after substantial interfacial contact is lost; it is conceivable that until a certain degree of surface contact is lost, the anode restricts the electrolyte from displacing vertically (Figure 6f). All of the data obtained from the local contact area and its variation with thermal cycling is displayed in Table V.

Tension-induced anode cracking.—The cell curvature is expected to induce tensile strain near the convex face and compressive strain

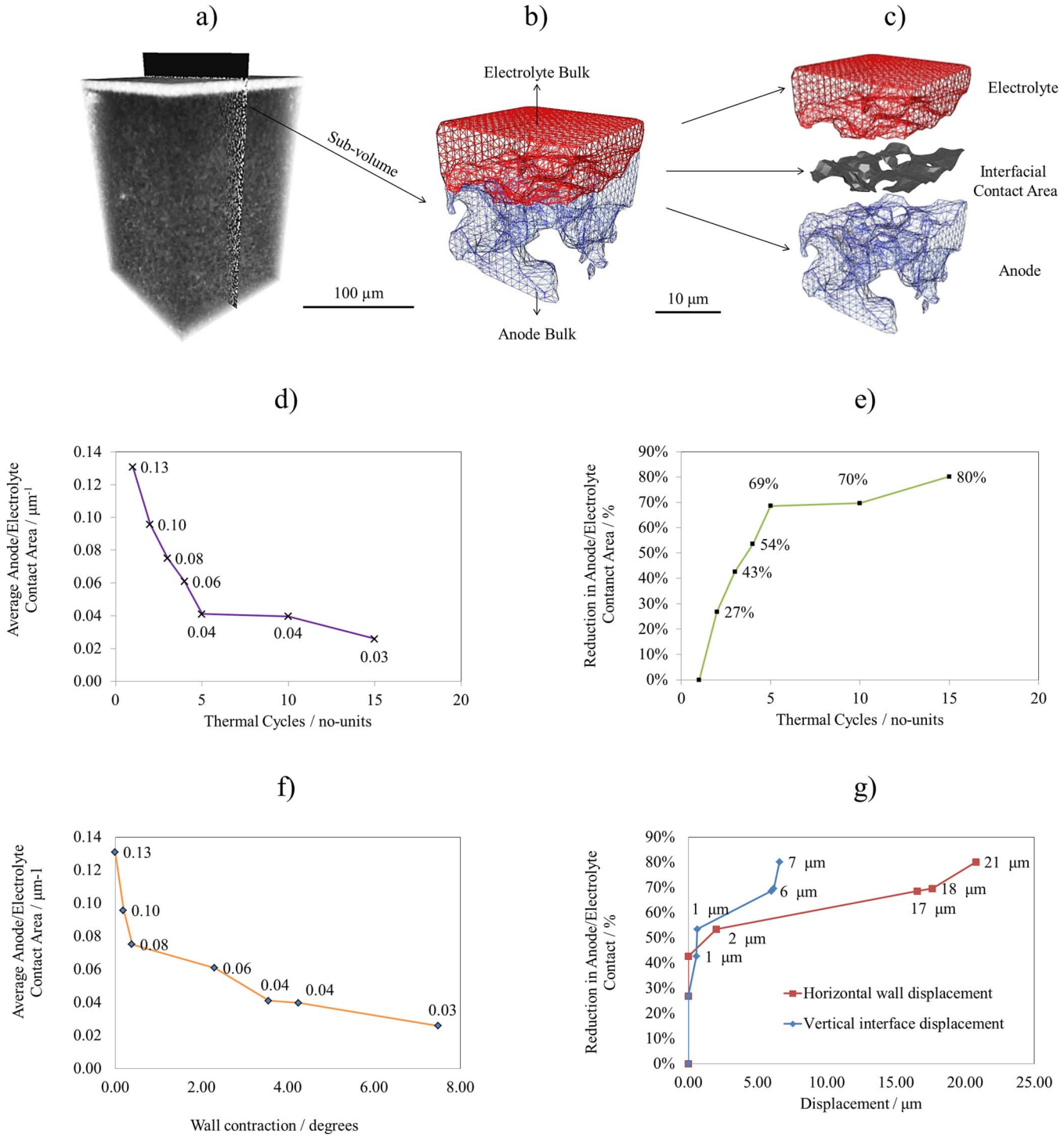

Figure 5. Interfacial contact between the anode and electrolyte assessed with thermal cycling: a) a greyscale volume render of a single 3D sub-volume from the first tomogram, b) a high-resolution surface generation, with c) exploded view of the anode (blue mesh)/electrolyte (red mesh) interface (gray surface), d) the variation and e) reduction in the anode/electrolyte contact area, volume corrected and plotted with respect to the number of thermal cycles, f) the variation in the anode/electrolyte contact area, volume corrected and plotted with respect to the cell-wall contraction angle, and g) the reduction in the anode/electrolyte contact area plotted with respect to the horizontal and vertical cell displacements.

near to the concave face. In this set-up the anode would be expected to experience tensile strain, and the electrolyte compressive strain, both of which would be anticipated to increase with the accumulative curvature. Although compressive strain may be difficult to observe without crystallographic information, sufficient tensile strain may induce cracking which, if imaged with sufficient resolution like that which has been done here, may be mapped and quantified using X-ray CT.

Fracture mechanics are known to occur across multiple length scales through a wide range of mechanisms which are specific to the crack stimulus and the materials under investigation.[32] The cracking within the anode is therefore mapped and quantified using both

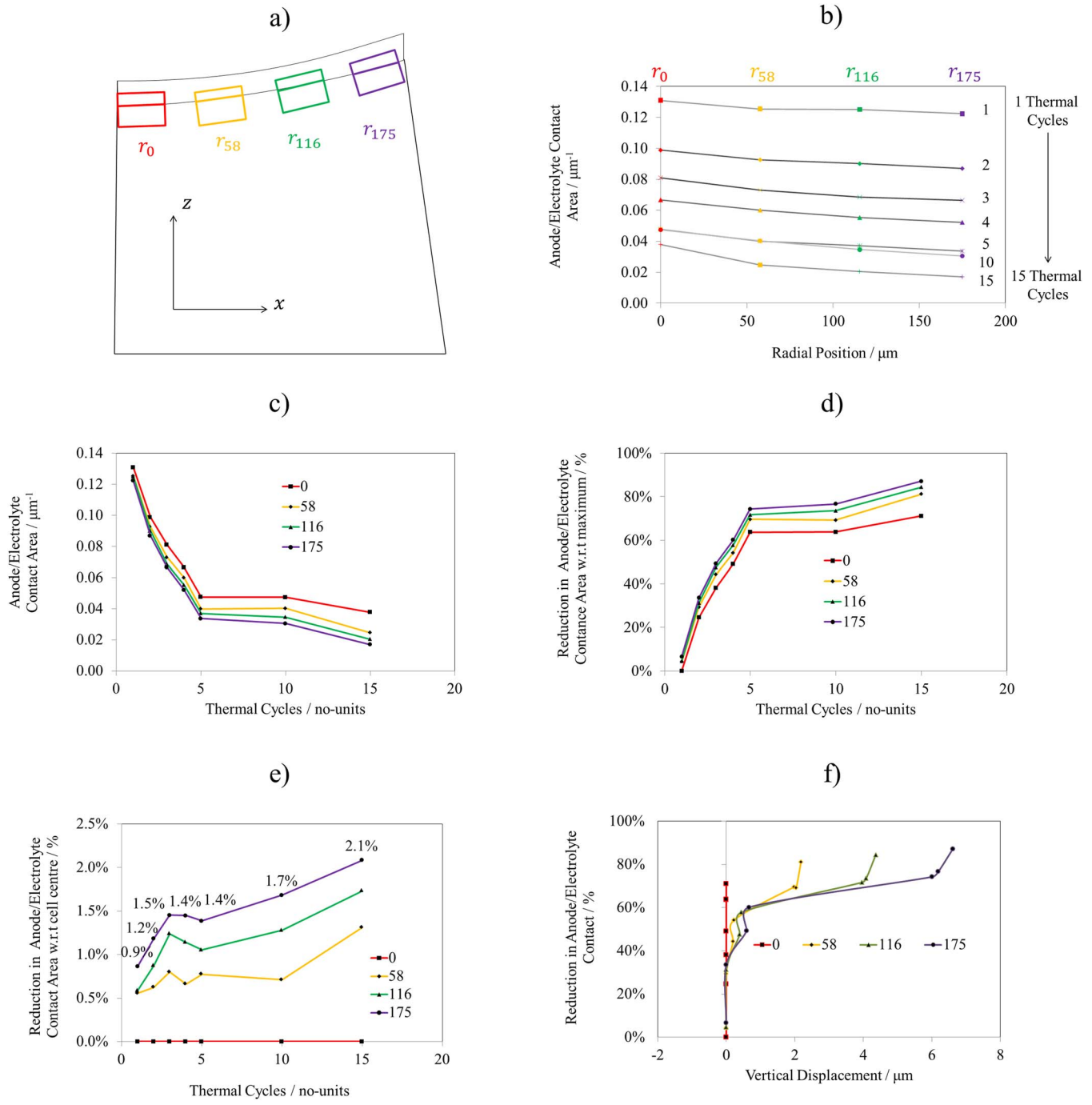

Figure 6. Radial variation in the volume specific anode/electrolyte interfacial contact area with thermal cycling: a) color-coordinated spatial reference for the four sub-volumes removed from each tomogram, b) variation in the volume-corrected anode/electrolyte contact area plotted with respect to the radial position for each thermal cycle: 1, 2, 3, 4, 5, 10 and 15 cycles d) variation in volume-corrected anode/electrolyte contact area plotted with respect to the number of thermal cycles for each radial position: at 0, 58, 116 and 175 µm from the cell center, e) the reduction in interfacial contact with respect to the center of the initial tomogram, f) the reduction in the interfacial contact with respect to the local vertical displacement of the cell, and g) the reduction in the interfacial contact with respect to the contact at the center of each tomogram. Radial positions 0, 58, 116 and 175 µm are represented throughout in red, orange, green and purple respectively.

micro- and nano-CT allowing a multi-length scale comparison. Due to the trade-off between imaging resolution and FOV, multi-length scale CT is employed so that the cracks imaged by nano-CT increase the detectable size-range and are complemented by the cracks imaged by micro-CT which captures a more complete crack morphology. The crack-diameter histograms for the nano- and micro-CT tomograms (Figure 7d) follow a similar pattern; crack diameters cluster around 3 – 4 µm (Figure 7d). A cluster also occurs at around 1 µm for the nano-CT, likely beyond the resolution limits of the micro-CT, and at 7 µm and 10 µm for the micro-CT, likely beyond the sample volume limits for nano-CT.

To inspect the mechanisms responsible for crack propagation several cracks are inspected individually. A general trend is observed that longer cracks display a larger average crack diameter (Figure 7e) although, the local diameter decreases from the crack-opening to crack-tip regardless of crack length (Figures 7f–7k). Crack propagation can follow many complex mechanisms and although displaying a general decrease the crack diameters also displayed

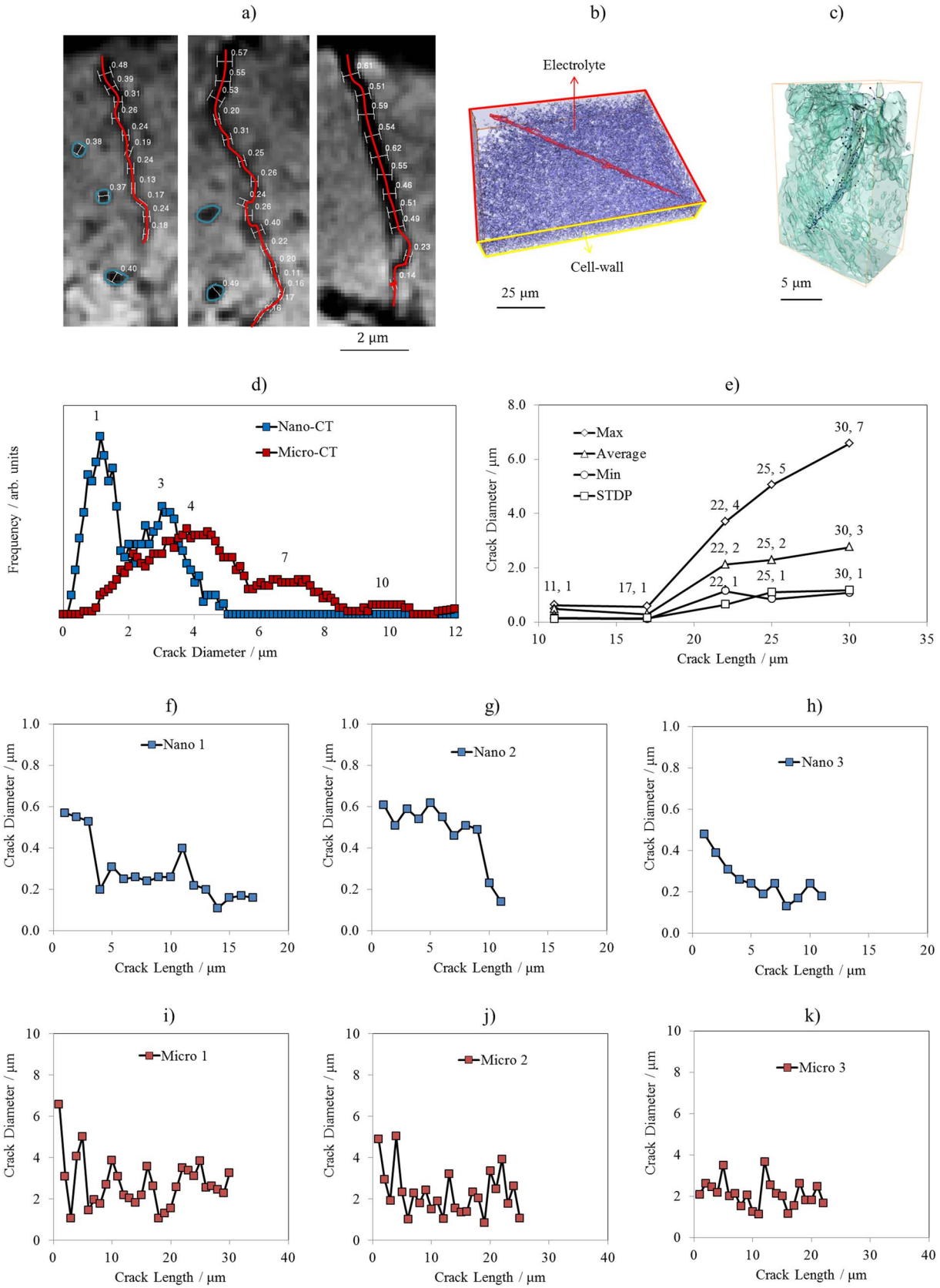

Figure 7. Mapping anode cracking across multiple length scales using micro- and nano-CT: a) three greyscale tomogram slices from the nano-CT, mapping cracks and their local diameters, b) micro-CT and c) nano-CT 3D surface generations from solid and crack phase segmentations, with accompanying crack diameter histogram for all detectable cracks, d) average crack diameter plotted with respect to the observable crack length for seven individual cracks, and e) accompanying standard deviation. Local diameter plotted with respect to crack length from the crack-opening to crack-tip for g – i) three nano-CT and j – l) three micro-CT cracks. Micro- and nano-CT are represented throughout by red and blue respectively.

Table V. The reduction in the anode/electrolyte contact area with both radial position and thermal cycles calculated with respect to the center of the initial tomogram.

Thermal Cycles/no-units	1	2	3	4	5	10	15
Radial Position = 0 μm	0%	25%	38%	49%	64%	64%	71%
Radial Position = 58 μm	4%	29%	44%	54%	70%	69%	81%
Radial Position = 116 μm	4%	31%	48%	58%	72%	74%	84%
Radial Position = 175 μm	7%	34%	49%	60%	74%	77%	87%

Table VI. Crack properties for six cracks from the SOFC anode after thermal cycling collected from micro- and nano-CT microstructural post-mortem analyses.

	Micro 1	Micro 2	Micro 3	Nano 1	Nano 2	Nano 3
Crack Length/μm	30.0	25.0	22.0	17.0	11.0	11.0
Maximum Diameter/μm	6.6	5.0	3.7	0.6	0.6	0.5
Average Diameter / μm	2.8	2.3	2.1	0.3	0.5	0.3
Minimum Diameter / μm	1.1	0.8	1.1	0.1	0.1	0.1
Standard Diameter Deviation/no-units	1.2	1.1	0.6	0.1	0.1	0.1

significant undulation due to bottlenecks and openings (Figures 7f–7k). Fewer undulations are detected in the nano-CT due to the shorter crack lengths 10−15 μm compared to the micro-CT which are around double the length, 20−30 μm. Regardless of crack length, the gradient of the linear fitting remains on the same order of magnitude for all cracks, between −0.02 and −0.04 μm diameter/μm length. The crack properties for the six cracks inspected in detail are tabulated in Table VI.

Although insight has been gained into the propagation of cracking within the anode, all cracks which were detected were found within the anode bulk, away from the anode/electrolyte interface, therefore the implications of curvature-induced anode cracking may be minor until cracking propagates toward the functional layer. This lack of cracking near the interface is thought to be attributed to the strain distribution within the cell; the tensile strain within the anode will be maximized away from the convex of the interface. It was more difficult to apply confident spatial orientation to the nano-CT due to the sub-volume size; the nano-CT no longer had the electrolyte as a spatial reference therefore the orientation relative to working cell operation was difficult to obtain. However, all of the cracks detected within the micro-CT were dominated by propagation parallel to the interface; i.e. cracks within the anode support layer typically propagated to the cell-wall rather than the interface (Figure 7b), therefore even after propagation, cracking may not influence activity within the functional region of the anode. However, large cracking may influence the effective local gas diffusivities and the ability for current removal.

Conclusions

This work concludes the second piece of a two-part study on thermally induced degradation within SOFCs. Delamination of the ceramic electrolyte from the cermet anode is a known cause of performance loss and is largely attributed to an inability to withstand mismatches in thermal expansion during operational thermal cycling. Through the use of non-destructive 3D characterization techniques to obtain macroscopic surface and internal metrics, a comprehensive understanding of the mechanisms responsible for mechanical performance losses attributed to cell delamination are elucidated and the implications on electrochemical performance are proposed.

Macroscopic deformation proceeds gradually with thermal ramping until a critical point is passed induced in this case through the use of rapid thermal ramp-rates, after which permanent deformation is observed in the form of a substantial curvature of the electrolyte at the interface and contraction of the cell-wall. Furthermore, cell-wall contraction angles suggest that the distribution within the anode layers may not be uniform possibly providing further mechanisms for performance loss. Microscopic interfacial contact between the anode and electrolyte decreases substantially after each thermal cycle but most considerably after the macroscopic deformation. Moreover, the anode contact varies across the radius of the cell whereby the contact is minimal at the cell wall and the deviation between the cell-center and cell-wall increases with each thermal cycle, exacerbating the stress gradient. The tensile strain which the anode experiences during interfacial curvature may be responsible for anode cracking. Such cracks are expected to increase in diameter with increase length propagated, possibly implicating phase percolation and structural integrity, although, cracks have only been observed within the anode bulk and parallel to the interface and therefore may not propagate toward the functional layer thus, electrochemical implications may be minor. It should be noted that this cell does not possess a cathode layer; additional materials that expand with other thermal expansion coefficients may result in additional degradation and strain distributions however, the anode/electrolyte expansion mismatch is considered to be the most severe.

This work investigates the effects of thermal cycling on the anode/electrolyte contact area and its possible implications on electrochemical performance. With use of lab-based X-ray CT instruments, high-resolution structural analyses of the same sample between exposures to operationally relevant thermal treatments has provided insight into the implications of rapid start-up times for planar anode-supported solid oxide fuel cells. Delamination is an issue not limited to fuel cell applications but many areas where thermal expansion mismatch proves problematic. This work will therefore also provide as a basis for comparable studies to further understating of material degradation across broader fields.

Acknowledgments

The authors acknowledge the EPSRC (EP/M014045/1, EP/P009050/1), the Centre for Doctoral training (EP/L015749/1) and the Royal Academy for Engineering for financial support, access to the Zeiss Xradia 520 Versa instrument was supported by EPSRC (EP/N032888/1) and access to the Zeiss Xradia 810 Ultra instrument was supported by the EPSRC (EP/K005030/1) and (EP/P009050/1).

ORCID

T. M. M. Heenan https://orcid.org/0000-0001-9912-4772
J. B. Robinson https://orcid.org/0000-0002-6509-7769
D. J. L. Brett https://orcid.org/0000-0002-8545-3126
P. R. Shearing https://orcid.org/0000-0002-1387-9531

References

1. N. P. Brandon and D. J. Brett, "Engineering porous materials for fuel cell applications. Philosophical Transactions of the Royal Society of London A: Mathematical," *Physical and Engineering Sciences*, **364**(1838), 147 (2006).
2. Y. C. Hsiao and J. R. Selman, "The degradation of SOFC electrodes." *Solid State Ionics*, **98**(1), 33 (1997).
3. L. Blum, "An Analysis of Contact Problems in Solid Oxide Fuel Cell Stacks Arising from Differences in Thermal Expansion Coefficients." *Electrochimica Acta*, **223**, 100 (2017).
4. X. Lu, T. M. Heenan, J. J. Bailey, T. Li, K. Li, D. J. Brett, and P. R. Shearing, "Correlation between triple phase boundary and the microstructure of Solid Oxide Fuel Cell anodes: The role of composition, porosity and Ni densification." *Journal of Power Sources*, **365**, 210 (2017).
5. M. Pihlatie, A. Kaiser, and M. Mogensen, "Mechanical properties of NiO/Ni–YSZ composites depending on temperature, porosity and redox cycling." *Journal of the European Ceramic Society*, **29**(9), 1657 (2009).
6. S. Celik, B. Ibrahimoglu, S. Toros, and M. D. Mat, "Three dimensional stress analysis of solid oxide fuel cell anode micro structure." *International Journal of Hydrogen Energy*, **39**(33), 19119 (2014).
7. M. Radovic, E. Lara-Curzio, R. M. Trejo, H. Wang, and W. D. Porter, "Thermophysical properties of YSZ and Ni-YSZ as a function of temperature and porosity."

Advances in Solid Oxide Fuel Cells II: Ceramic Engineering and Science Proceedings, Cocoa Beach, **27**(4), 79 (2009).
8. M. Mori, T. Yamamoto, H. Itoh, H. Inaba, and H. Tagawa, "Thermal Expansion of Nickel-Zirconia Anodes in Solid Oxide Fuel Cells during Fabrication and Operation." *Journal of the Electrochemical Society*, **145**(4), 1374 (1998).
9. A. Atkinson and B. Sun, "Residual stress and thermal cycling of planar solid oxide fuel cells." *Materials Science and Technology*, **23**(10), 1135 (2007).
10. T. M. M. Heenan, J. B. Robinson, X. Lu, B. Tjaden, A. Cervellino, J. J. Bailey, D. J. L. Brett, and P. R. Shearing, "Understanding the thermo-mechanical behavior of solid oxide fuel cell anodes using synchrotron X-ray diffraction." *Solid State Ionics*. (2017).
11. J. B. Robinson, L. D. Brown, R. Jervis, O. O. Taiwo, T. M. Heenan, J. Millichamp, T. J. Mason, T. P. Neville, R. Clague, D. S. Eastwood, and C. Reinhard, "Investigating the effect of thermal gradients on stress in solid oxide fuel cell anodes using combined synchrotron radiation and thermal imaging." *Journal of Power Sources*, **288**, 473 (2015).
12. R. Clague, P. R. Shearing, P. D. Lee, Z. Zhang, D. J. L. Brett, A. J. Marquis, and N. P. Brandon, "Stress analysis of solid oxide fuel cell anode microstructure reconstructed from focused ion beam tomography." *Journal of Power Sources*, **196**(21), 9018 (2011).
13. J. R. Wilson, W. Kobsiriphat, R. Mendoza, H. Y. Chen, J. M. Hiller, D. J. Miller, K. Thornton, P. W. Voorhees, S. B. Adler, and S. A. Barnett, "Three-dimensional reconstruction of a solid-oxide fuel-cell anode." *Nature materials*, **5**(7), 541 (2006).
14. P. R. Shearing, J. Gelb, and N. P. Brandon, "X-ray nano computerised tomography of SOFC electrodes using a focused ion beam sample-preparation technique." *Journal of the European Ceramic Society*, **30**(8), 1809 (2010).
15. T. M. M. Heenan, J. J. Bailey, X. Lu, J. B. Robinson, F. Iacoviello, D. P. Finegan, D. J. L. Brett, and P. R. Shearing, "Three-Phase Segmentation of Solid Oxide Fuel Cell Anode Materials Using Lab Based X-ray Nano-Computed Tomography." *Fuel Cells*, **17**(1), 75 (2017).
16. Z. Shao and S. M. Haile, "A high-performance cathode for the next generation of solid-oxide fuel cells." *Nature*, **431**(7005), 170 (2004).
17. H. Itoh, T. Yamamoto, M. Mori, T. Horita, N. Sakai, H. Yokokawa, and M. Dokiya, "Configurational and electrical behavior of Ni-YSZ cermet with novel microstructure for solid oxide fuel cell anodes." *Journal of the Electrochemical Society*, **144**(2), 641 (1997).
18. X. Lu, T. Li, O. O. Taiwo, J. Bailey, T. Heenan, K. Li, D. J. L. Brett, and P. R. Shearing, "June. Study of the tortuosity factors at multi-scale for a novel-structured SOFC anode." In *Journal of Physics: Conference Series* **849**(1), 012020 (2017). IOP Publishing.
19. S. Tao and J. T. Irvine, "A redox-stable efficient anode for solid-oxide fuel cells." *Nature materials*, **2**(5), 320 (2003).
20. S. Timoshenko, "Analysis of bi-metal thermostats." *JOSA*, **11**(3), 233 (1925).
21. X. Lu, S. D. Rawson, and P. J. Withers, "Effect of hydration and crack orientation on crack-tip strain, crack opening displacement and crack-tip shielding in elephant dentin." *Dental Materials*, (2018).
22. V. Julie, L. Jérôme, C. Peter, B. Pierre, D. Gérard, S. Heikki, and U. V. François, "3D phase mapping of solid oxide fuel cell YSZ/Ni cermet at the nanoscale by holographic X-ray nanotomography." *Journal of Power Sources*, **243**, 841 (2013).
23. J. Laurencin, R. Quey, G. Delette, H. Suhonen, P. Cloetens, and P. Bleuet, "Characterisation of Solid Oxide Fuel Cell Ni–8YSZ substrate by synchrotron X-ray nano-tomography: from 3D reconstruction to microstructure quantification." *Journal of Power Sources*, **198**, 182 (2012).
24. J. Laurencin, G. Delette, F. Lefebvre-Joud, and M. Dupeux, "A numerical tool to estimate SOFC mechanical degradation: case of the planar cell configuration." *Journal of the European Ceramic Society*, **28**(9), 1857 (2008).
25. T. M. Heenan, J. B. Robinson, X. Lu, J. J. Bailey, D. J. Brett, and P. R. Shearing, "Analyzing the Mechanical Performance of Solid Oxide Fuel Cells at Interfacial Anode/Electrolyte Regions Using Sub-Micron Resolution 3D X-Ray Computed Tomography." *ECS Transactions*, **78**(1), 2317 (2017).
26. T. M. M. Heenan, D. P. Finegan, B. Tjaden, X. Lu, F. Iacoviello, J. Millichamp, D. J. Brett, and P. R. Shearing, "4D nano-tomography of electrochemical energy devices using lab-based X-ray imaging." *Nano Energy*, **47**, 556 (2018).
27. J. J. Bailey, T. M. M. Heenan, D. P. Finegan, X. Lu, S. R. Daemi, F. Iacoviello, N. R. Backeberg, O. O. Taiwo, D. J. L. Brett, A. Atkinson, and P. R. Shearing, "Laser-preparation of geometrically optimised samples for X-ray nano-CT." *Journal of Microscopy*, (2017).
28. S. J. Cooper, A. Bertei, P. R. Shearing, J. A. Kilner, and N. P. Brandon, "TauFactor: An open-source application for calculating tortuosity factors from tomographic data." *SoftwareX*, **5**, 203 (2016).
29. T. Walter and J. C. Klein, "October. Segmentation of color fundus images of the human retina: Detection of the optic disc and the vascular tree using morphological techniques." *In International Symposium on Medical Data Analysis*, 282 (2001). Springer, Berlin, Heidelberg.
30. C. Pudney, "Distance-ordered homotopic thinning: a skeletonization algorithm for 3D digital images." *Computer Vision and Image Understanding*, **72**(3), 404 (1998).
31. O. O. Taiwo, D. P. Finegan, D. S. Eastwood, J. L. Fife, L. D. Brown, J. A. Darr, P. D. Lee, D. J. Brett, and P. R. Shearing, "Comparison of three-dimensional analysis and stereological techniques for quantifying lithium-ion battery electrode microstructures." *Journal of microscopy*, **263**(3), 280 (2016).
32. P. J. Withers, "Fracture mechanics by three-dimensional crack-tip synchrotron X-ray microscopy." *Phil. Trans. R. Soc. A*, **373**(2036), 20130157 (2015).